Journal of Nuclear Materials 393 (2009) 162–174

Contents lists available at ScienceDirect

Journal of Nuclear Materials

journal homepage: www.elsevier.com/locate/jnucmat

Towards a more comprehensive microstructural analysis of Zr–2.5Nb pressure tubing using image analysis and electron backscattered diffraction (EBSD)

P. Hovington [a,*], P.T. Pinard [b], M. Lagacé [a], L. Rodrigue [a], R. Gauvin [b], M.L. Trudeau [a]

[a] Materials Science, Institut de recherche d'Hydro-Québec, 1800 Lionel-Boulet, Varennes, Quebec, Canada J3X 1S1

[b] Mining and Materials Engineering Department, McGill University, 3610 University St., Montreal, Quebec, Canada H3A 2B2

ARTICLE INFO

Article history:
Received 6 April 2009
Accepted 28 May 2009

PACS:
68.37.Hk
87.64.Ee
61.05.J
87.57.N
61.72.Mm
68.55.jm

ABSTRACT

Zr–2.5Nb pressure tubes used in CANDU (CANada Deuterium Uranium) reactors have a very complex microstructure, with two major crystallographic phases, α and β. These phases include a fair amount of deformation from the extrusion process and the cold working (~25%) performed at the end of the manufacturing process. This microstructure (texture, grain aspect ratio, etc.) changes along the tube's length and differs from tube to tube. In order to better understand the deformation mechanisms, these microstructural differences must be statistically characterized. Scanning electron microscopy combined with direct image analysis or with electron backscattered diffraction (EBSD) are good techniques for carrying out such a measurement. However it is not possible, using specimen preparation methods specific for each of these techniques, to reveal all of the grain and phase boundaries. We have thus developed post-treatment algorithms to be able to partially analyze the revealed Zr–2.5Nb microstructure. The first algorithm was used for image analysis treatments of micrographs taken at 5 kV on the radial–tangential plane of etched samples using a reactive ion etch (RIE, $CF_4 + O_2$). The second was developed for EBSD grain mapping and can be used to characterize α-Zr grain shape and orientation. The two techniques are complementary: EBSD gives information about the micro-texture and the relationship between the microstructure and micro-texture while image analyses of SEM micrographs reveal the direction and distribution of the α-Zr lamellae more easily and over a greater sample area than EBSD. However, the SEM micrographs that were used did not reveal any grain boundary (only phase boundary). An analysis of EBSD grain maps reveals that the average α-Zr grain size, mainly in the elongated direction (tangential), is smaller than what is normally obtained from an image analysis of SEM micrographs. The grain size distribution of type I α-Zr grains (deformed original (prior) α-Zr) and type II (stress-induced β-Zr → α-Zr phase transformation) is also shown to be different for sizes greater than 0.4 μm^2.

1. Introduction

About 400 pressure tubes made of a Zr alloy containing 2.5 wt% Nb are the heart of the CANDU-6 reactor [1]. The pressure tubes hold the uranium fuel rods along with the heat-transport fluid used to extract the energy from the nuclear reaction. Their deformation governs the power output and thus the reactor's lifespan [2]. In service, radial stresses are applied to the inner wall by pressure from the heat-transport fluid. The tubes are also subjected to flexing stresses caused by the weight of the uranium fuel and the heat-transport fluid. Combined with the constant heat coming from the nuclear reaction (250 °C at the inlet and up to 300 °C at the outlet) and the neutron flux, those stresses cause the pressure tubes to deform (diametral creep, elongation and sagging). Diametral creep is the most critical process. When the amount of strain reaches a maximum limit, the tube must be decommissioned thus limiting the available output and the profitability of the reactor [3].

The Zr–2.5Nb alloy is composed of two primary phases: an α-Zr phase composed of nearly pure zirconium and a β-Zr phase that contains up to 40% niobium. Pressure tubes are made by extrusion, which results in a highly textured α-Zr microstructure [4]. Because the extrusion is done near the β-Zr to α-Zr transformation temperature, the microstructure can be quite different between the tubes and even along a single tube's length [5]. Measurements conducted in power plants show that pressure tubes made of the same alloy can exhibit very different deformations over time for similar operating conditions [6]. This is an indication that the pressure tube's microstructure can play an important role in tube deformation. There are a lot of efforts and a great economical driving force to predict the creep behavior of Zr–2.5Nb pressure tubes. Many parameters are analyzed such as the texture, level of impurities, etc. However, microstructural parameters (e.g. grain size, aspect ratio) are less used because they are more difficult to measure

---

* Corresponding author. Tel.: +450 652 8125; fax: +450 652 8424.
E-mail address: hovington.pierre@ireq.ca (P. Hovington).

0022-3115/$ - see front matter Crown Copyright © 2009 Published by Elsevier B.V. All rights reserved.
doi:10.1016/j.jnucmat.2009.05.017

and quantify. This paper is a contributing effort on the development of techniques for the microstructural characterization of the main crystalline phase (α-Zr) of Zr–2.5Nb pressure tubes.

All the micrographs and maps in this paper are taken in the radial–tangential plane (Fig. 1(a)). Typical micrographs are shown in Fig. 1(b) and (c) where we clearly see the complex microstructure of the α-Zr grains (lamellae) separated by 'β-Zr' phase. In fact, the region identified as 'β-Zr' could be formed of several phases, namely metastable body centered cubic (bcc) β-Zr containing approximately 20% Nb, some α-Zr (equilibrium < 0.5% Nb), β-Zr (enriched in Nb to ~50%), ω-Zr (a metastable hcp phase of intermediate Nb content) and β-Nb (bcc containing ~95% Nb) [3]. In the present work, we will refer to this set as β′-Zr (β prime) to prevent any confusion since we are mainly interested in the α-Zr phase.

The main phase (α-Zr) has elongated grains typical of extrusion processes. The phase boundary between α-Zr and β'-Zr can be seen clearly in Fig. 1(b) and (c). However, the grain boundary along α-Zr lamellae is often not seen. Grain size analysis was traditionally done using the replica method in transmission electron microscopy. This method is very labor-intensive and covers only a very small area of the original pressure tube. This could bias the results as the microstructure is not homogeneous throughout the tube. Recently, we were able to develop an image analysis technique using SEM micrographs to extract quantitative data from partly revealed microstructures of Zr–2.5Nb pressure tubes [7]. However, this technique does not allow for direct measurement of α-Zr grain size. It is based on the average intercept length of a grid within the α-Zr phase grains. In this paper, electron backscattered diffraction (EBSD) is used to measure grain size and grain shape statistics from individual α-Zr grains. Comparison between the two techniques will also be covered.

EBSD was used by Holt and Zhao [8] for micro-texture measurements. However, because they were using a standard scanning electron microscope (thermal tungsten emitter), for which they estimated the resolution at 1 μm for EBSD measurement, they were not able to detect the finest grains and perform grain mapping. In this work, we will be using a cold field emission gun SEM with a better effective resolution.

2. Material and methods

2.1. Material

The pressure tube that was used was taken from a standard 2007 Nu-TECH production. The ingot chemistry is presented in Table 1. The ingot was heated to ~975 °C for ~1 h before being beta quenched. The reported amount of cold work was 25%. The pressure tube was put in an autoclave at 400 °C for 24 h for stress relief. It has been shown that this stress relief does not affect the micro-texture [8]. The sample studied comes from the front section of the tube.

Table 1
Chemical analysis for the Zr-2.5Nb pressure tube tested.

Element	Concentration
Niobium	2.7 wt%
Oxygen	1127 PPM
Aluminum	42 PPM
Hydrogen	<3 PPM
Iron	992 PPM
Si	<25 PPM
Carbon	59 PPM
Chromium	<100 PPM
Tanatalum	<100 PPM
Zirconium + other permissible impurities	Balance

2.2. Specimen preparation

Proper specimen preparation is paramount for both automated images analysis and EBSD. However, both techniques have special requirements that turn out to be incompatible. Image analysis needs a high contrast to be able to differentiate between α-Zr and β′-Zr phases using gray scale thresholding. EBSD needs a surface free of deformation induced by sample preparation and a very smooth surface to avoid shadowing effects during mapping. As a result, we developed very different specimen preparation techniques to perform both measurements.

For image analysis, we used a standard metallographic sample preparation down to 3 μm diamond paste with a final step of colloidal silica. To clearly reveal the β′-Zr phase, the sample was exposed to a $CF_4 + O_2$ plasma using the EA Fischione Instrument's Automatic Sample Preparation apparatus (ASaP) [9].

As with other hexagonal close-packed (HCP) metals, Zr–2.5Nb has low grinding and polishing removal rates, making the elimination of all polishing scratches and deformation difficult [10]. This represents a major challenge for EBSD characterization which necessitates a sample without deformation from the specimen preparation procedure. In addition, Zr is very reactive, leading to the formation of a thin layer of oxides and hydroxides on the surface of the specimen [11].

However, mechanical polishing alone cannot remove all of the plastic surface deformation. It must be followed by other techniques such as chemical etching, electro-polishing or ion beam

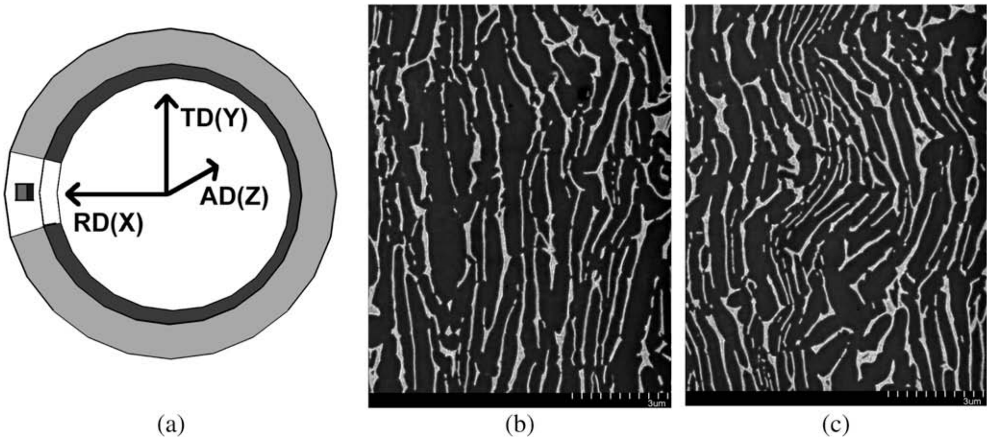

Fig. 1. Schematic representation of the texture found in Zr–2.5Nb pressure tubes (a) together with typical microstructures found in the radial–transverse plane (b and c). Radial direction of the tube is horizontal in both micrographs. (c) Shows some α-Zr that deviate from the typical tangent direction.

milling. Previous work involved either chemical etching [12] or electro-polishing [8] as a final step. However, it was found that both techniques preferentially remove α-Zr phase, which leaves β′-Zr ridges, thus greatly limiting the efficiency of EBSD mapping because of shadowing effects (Fig. 2). It is important to note that grain orientation mapping is more demanding on specimen preparation than texture analysis since the diffraction patterns must be indexed even near the grain boundaries [13].

We tried several different approaches to achieve an artifact-free, low-roughness surface. So far, the best technique combined an iterative polishing–etching technique [14] followed by broad ion beam etching. First, the sample was polished using a standard mechanical specimen preparation procedure. It was then etched using an acid solution of HF, HNO_3 and H_2O at room temperature. To remove the high roughness caused by the chemical etching, the sample was polished again using colloidal silica. Another chemical etching of approximately 20 s was then used to remove the last deformation layer. Next, the sample was un-mounted from the polishing resin and put in the ASaP for broad ion beam etching at glazing angle (<5°) and with low energy (<3 kV) to decrease its surface roughness. The latter process greatly decreases the plastic surface deformation and removes the roughness of the β′-Zr phase created by etching. Still, this technique does not efficiently prepare the constituent phases of β′-Zr for EBSD, especially in view of the small crystallite phase.

2.3. Experimental procedure for EBSD

The sample was mounted on a pre-tilted specimen holder to decrease stage drift caused by a heavy stage tilted at a high angle. A Hitachi S-4700 FEG-SEM was used at 15 keV in high magnification mode (15 kX). This microscope has a snorkel lens that extends the magnetic field outside the objective lens. This greatly increases the spatial resolution and the signal-to-noise ratio of the SE images. However, this magnetic field bends the trajectory of the backscattered electrons, which leads to distorted EBSD patterns. We used LisPix [15] to 'unwarp' the patterns before indexing. EBSD patterns of a silicon mono-crystal were taken at high and low magnification (where the external magnetic field found outside the objective lens is turned off) and were used to compute the amount of unwrapping necessary to compensate for the external magnetic field. The stored EBSD patterns were then unwrapped in batch. The EBSD pattern acquisition was performed with a Nordlys II camera and HKL Channel 5 software. The acquisition parameters were at 8 × 8 image binning, a dwell time of less than 20 ms and a step size of 30 nm. More than 1 000 000 EBSD patterns, taken from 18 mapped areas, were acquired and saved for this particular work.

2.4. Experimental procedure for image analysis

In order to get a direct comparison between this EBSD method and the image analysis method, the specimen was re-polished and etched for image analysis measurements. Using the same microscope and magnification, more than 200 micrographs were collected in approximately the same region as the EBSD maps using the upper secondary electron detector imaging (SEI). The micrographs for image analysis were taken using a beam energy of 5 kV in order to get a good contrast between the α-Zr and β′-Zr phases, compared to 15 kV for EBSD. The area measured using image analysis is about 13 times larger than the area covered by EBSD. The image analysis procedure was carried out using software developed at Hydro-Québec [16].

3. Results

3.1. Grain map analysis

Fig. 3 presents the band contrast (BC) of four scanned regions (out of 18) together with the BC histogram for all the regions. BC values are calculated for every pattern (indexed or not). Lower band contrast corresponds to regions which contain more diffuse (or no) Kikuchi patterns. A high level of detail is clearly displayed in the BC images, showing the β′-Zr phase in darker regions as well as the grain boundaries within the α-Zr phase. The BC histogram (Fig. 3(b)) clearly shows an overlap of two peaks (Gaussian). The first, centered around 30, corresponds to the non-indexed β′-Zr phase and the grain boundaries; the second, around 55, corresponds mainly to the indexed α-Zr phase. The reasoning behind this comes from the following: the β′-Zr phase has a lower band contrast because it is either too deformed (i.e. no diffraction) or there are overlapping diffraction patterns due to the small size of the different constituent crystals. The reverse of this argument accounts for the higher band contrast of the α-Zr grains. Preferential etching of the α-Zr phase is another explanation. This information is used to distinguish and process orientation maps for better grain size measurements.

Fig. 4 shows an untreated phase map showing both phases: α-Zr in red and β-Zr (not β′) in blue. We clearly see that we were able to identify some β-Zr crystals between the lamellae of the α-Zr phase. However, the indexation rate was very limited (~1%).

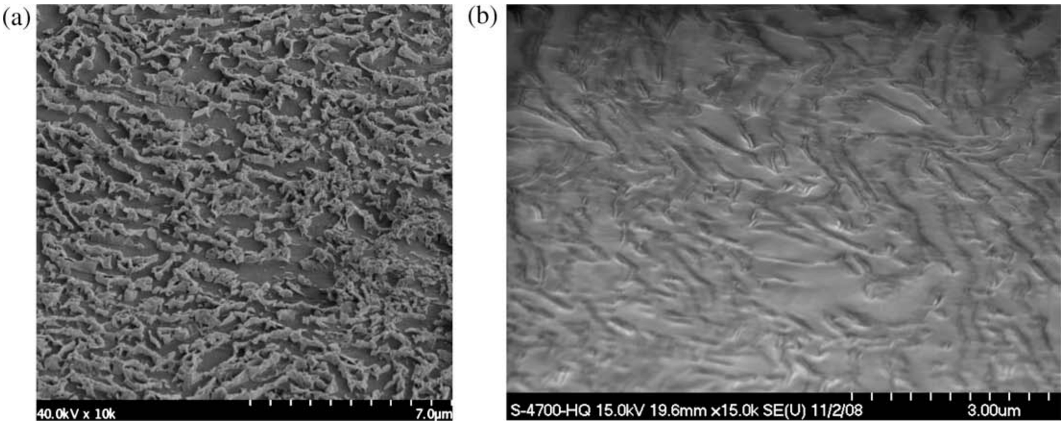

Fig. 2. SEM micrographs of Zr–2.5Nb viewed (a) after a chemical attack showing the ridges caused by the preferential etching of the α-Zr phase (tilt of 30°) and (b) after ion beam etching (tilt of 70°).

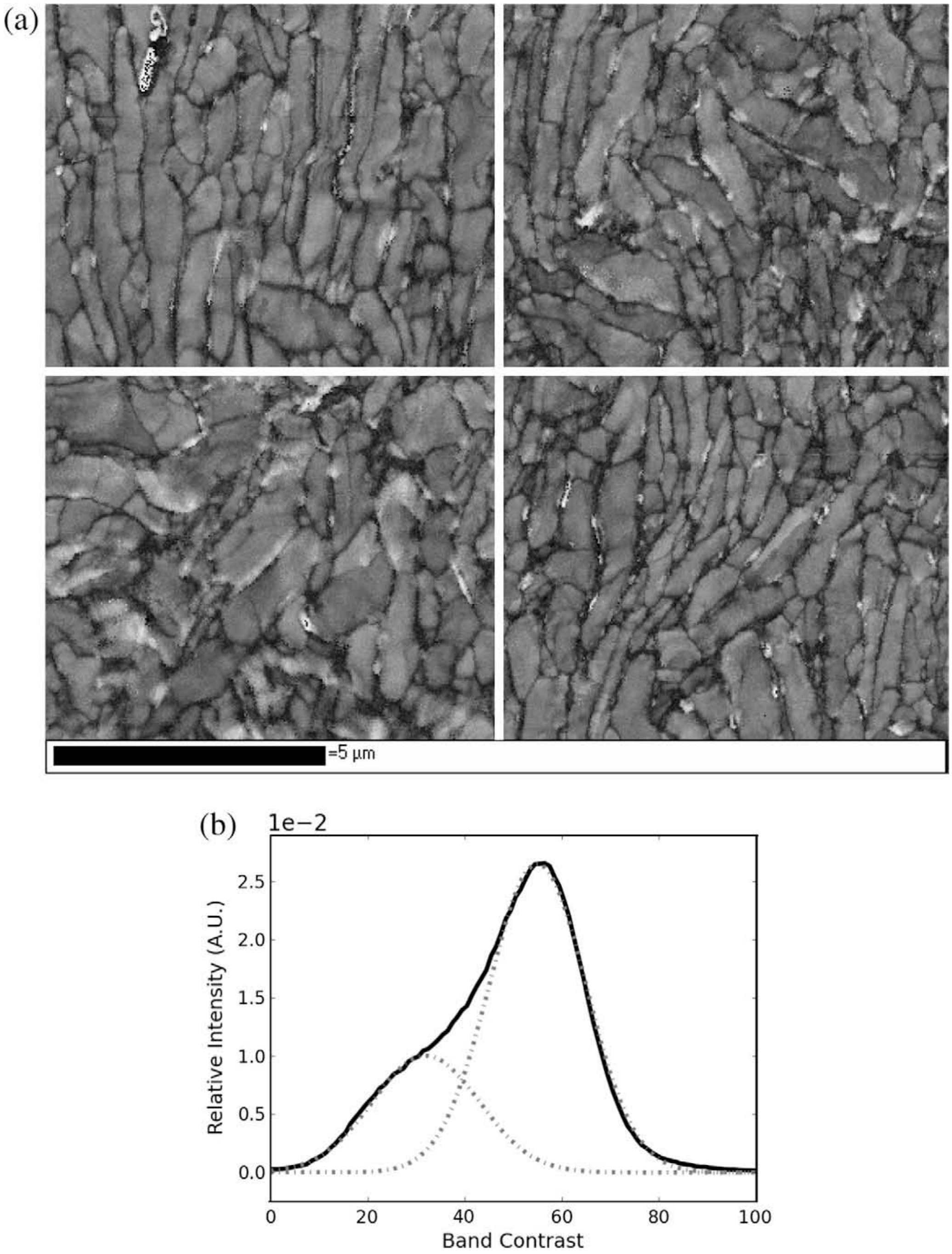

Fig. 3. In (a), band contrast (BC) images of four (4) out of 18 regions using EBSD as calculated by HKL Channel 5 software. (b) Presents the BC histogram covering the entire regions mapped (18 regions). The two fitted Gaussians are overlapped.

3.2. Extrapolation of non-indexed pattern for grain size measurement

To perform the grain analysis, the non-indexed pixels of the maps must be filled in. The first step consists in removing indexed patterns with a non-coherent solution compared to their adjacent patterns by using the procedure in HKL Channel 5 for removing the wild spikes. However, as mentioned previously, non-indexed pixels along grain and phase boundaries are unavoidable and have to be taken into account in the grain size analysis. A typical method is to iteratively increase the size of every grain until the grains' boundaries coalesce. This procedure, known as zero solution extrapolation in the HKL Channel 5 systems, has to be performed carefully, especially in the case of a multi-phase system. In this EBSD work, the inability to properly reveal enough of the β′-Zr phase (at least 15% of the map) complicates the post-processing procedure to correctly determine α-Zr grain size. Using extrapolation without considering the β′-Zr phase leads to larger and incorrectly shaped α-Zr grains. To overcome the non-indexation of the β′-Zr phase, a procedure was developed to identify the β′-Zr phase using the band contrast image.

The procedure makes the assumption that the low band contrast pixels correspond to the β′-Zr phase as explained previously. Therefore, the first step is to extract the low band contrast pixels by using a threshold of around 30 (Fig. 5(a)), which corresponds to the maximum intensity of the low contrast peak in the BC histogram (Fig. 3(b)). This number can vary with experimental

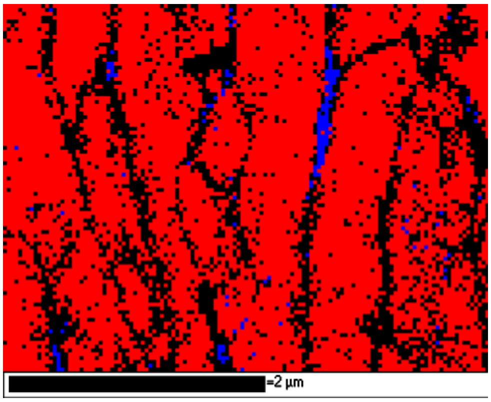

Fig. 4. Untreated phase map showing the β-Zr phase in blue and the α-Zr phase in red. Black regions correspond to non-indexed patterns.

conditions but it was constant for all of the 18 maps recorded and treated. All these pixels (except those that were previously indexed as α-Zr) are assigned to the β'-Zr phase and are then reintegrated in the original map (Fig. 5(b)). Zero solution extrapolation is then performed solely on the β'-Zr (Fig. 5(c)). Finally, extrapolation of the α-Zr grains (Fig. 5(d)) takes care of the non-indexed pattern inside α-Zr.

The effect of this grain reconstruction procedure is displayed in Fig. 6 where the size of a grain is shown before any extrapolation (a), after a rough extrapolation without taking into account the β'-Zr phase (b) and after the procedure explained above (c). More importantly, we clearly see in Fig. 6 that the shape and the orientation of the α-Zr grain are preserved. The shape and orientation of the α-Zr grains are believed to be among a number of major creep modeling parameters [3].

3.3. Grain mapping using treated orientation images

Fig. 7 presents the phase map results from the same four (4) regions as Fig. 3. The α-Zr regions (red) in Fig. 7 matches the high band contrast regions of Fig. 3.

In Fig. 8, we present an α-Zr grain map together with the elliptical fit for grains in random colour in (a), coloured according to the orientation towards the radial direction in (b), and coloured according to the orientation towards the tangential direction in (c). Both Fig. 8(b) and (c) use the colour code defined in (d). Even though the extrapolation is not perfect, a good match is found for most of the grains. The arrows show two grains that were identified as one as a result of a missing phase boundary. We are currently working on a new procedure that combines several maps (e.g. band contrast map, orientation map) to obtain more accurately extrapolated maps.

Assuming a proper identification of the α-Zr phase, several distributions can be computed. For this application, the distribution of the aspect ratio and that of the orientation of the long axis of the fitted ellipses (slope) are of greatest interest. Fig. 9 presents the distributions calculated for all 18 maps. Fig. 9(a) clearly shows that the mean aspect ratio has a maximum value higher than 1.5, which means that most of the width of the α-Zr grains (in the radial direction) is around one and a half times the length. This result is important since it is close to our image analysis results, which were not based on direct grain measurements but on intercept methods [7].

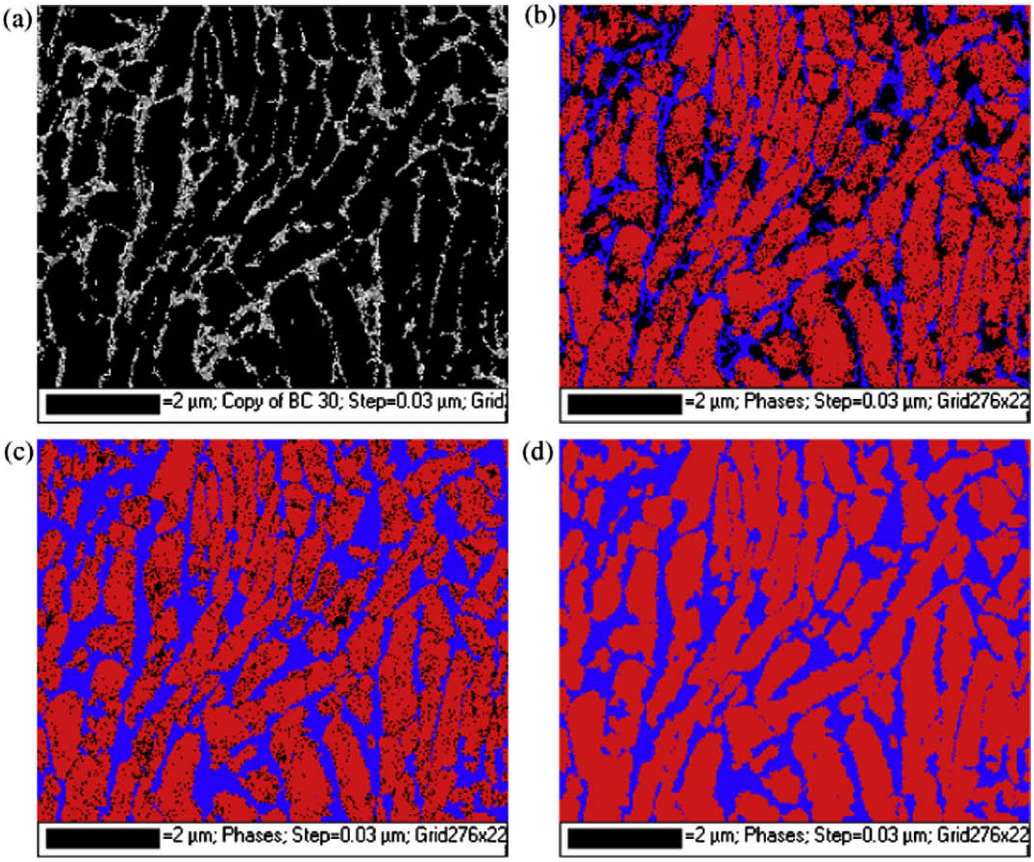

Fig. 5. Grain reconstruction procedure. In (a), BC image with band contrast between 0 and 30 in white. These pixels will be assigned to the β'-Zr phase; (b) the resulting phase images where the α-Zr grains are coloured in red and the β'-Zr grains are in blue; (c) the phase map after extrapolation of only the β'-Zr grains and (d) the complete phase map after extrapolation of only the α-Zr grains.

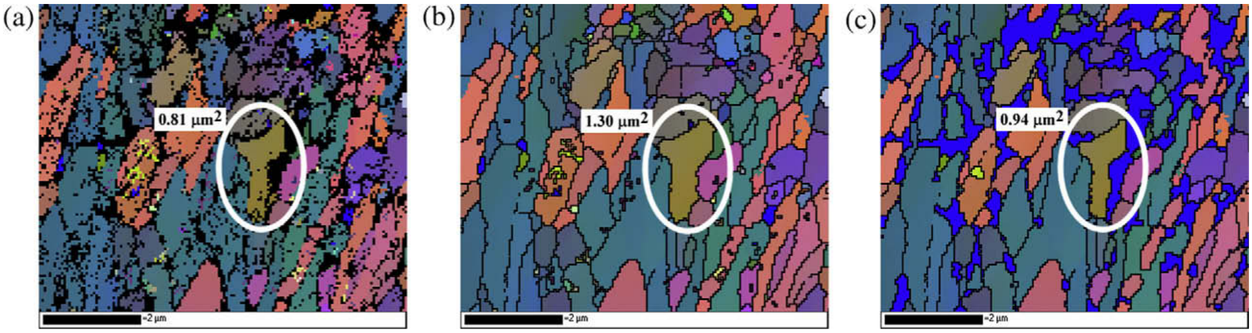

Fig. 6. Effect of grain reconstruction on grain size measurement (a) without any extrapolation, (b) after a rough extrapolation without taking into account the β′-Zr phase and (c) with the proposed procedure.

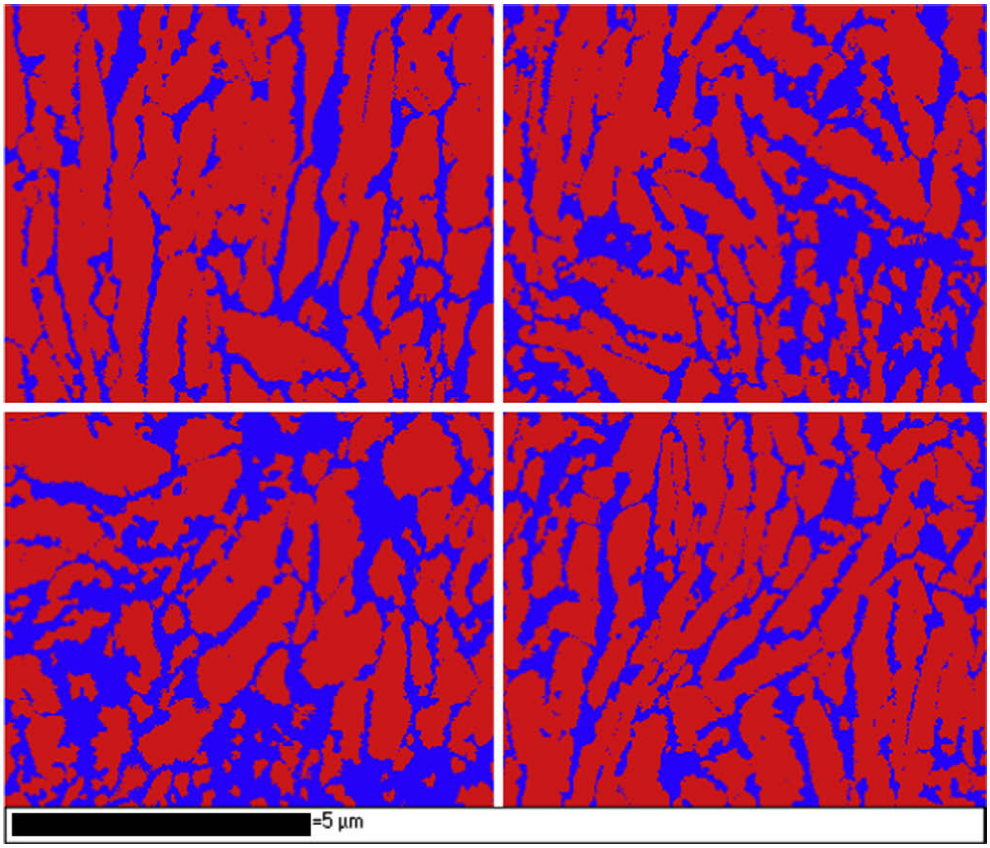

Fig. 7. Phase map of the extrapolated map for the four test regions. (red = α-Zr; Blue = β′-Zr).

To our knowledge, this is the first time that such measurements have been performed with fairly good statistics (more than 3000 α-Zr grains). Fig. 9(b) shows the maximum of the long axis of the grains (fitted ellipse) toward 90°, corresponding to the tangential direction with a Full Width at Half Maximum (FWHM) of around 40°. In addition, we can clearly see in Fig. 9(c) that the grains oriented toward the tangent direction have a significantly higher aspect ratio (up to 10×) and are bigger (up to 10 μm^2) (Fig. 9(d)). It is also important to note that those measurements were made by combining all the grains, including border grains. This could slightly bias the absolute results. However, the general trend is maintained.

3.4. Comparison with image analysis

Fig. 10 presents typical SEM micrographs made for image analysis (a–b) and typical EBSD grain maps (c–d) obtained using the method described earlier. In the grain maps, the β′-Zr phase is white and the phase and grain boundaries are marked red. In the SEM micrographs, the boundaries are also coloured red and superimposed on to the secondary electron micrograph (QC maps, see [7]). The image analysis micrographs reveal the phase boundaries but do not show any α-Zr boundaries. In the EBSD grain maps, both phase and α-Zr grain boundaries are present.

Using all of the micrographs made for the image analysis ($n = 240$) and the EBSD grain maps calculated using image analysis ($n = 18$), the anisotropy of the α-Zr grains (Fig. 11) can be measured using the same image analysis algorithm [7]. Table 2 shows the half-length of the major and minor axis of the mean intercept length presented in Fig. 11 for the EBSD gain maps and the SEM micrographs. Both measurements show elongated ellipses in the tangential direction, indicating an elongated microstructure in this direction. A higher discrepancy can be seen in the tangential direction (long axis), which shows a lower mean intercept length

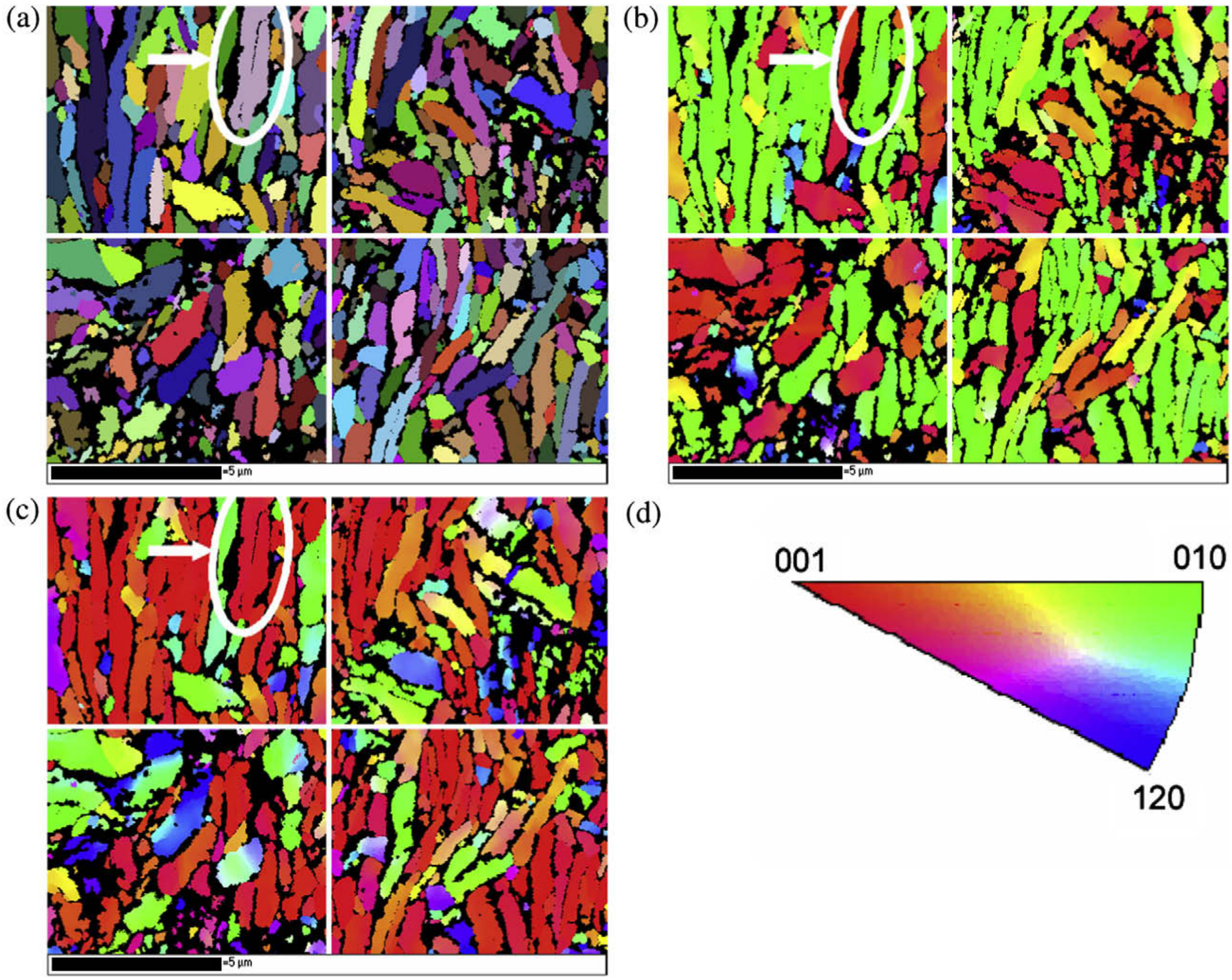

Fig. 8. Orientation map of the α-Zr grains (a) random colour grains, (b) coloured according to the orientation towards radial direction, (c) coloured according to the orientation towards the tangent direction. Both (b) and (c) are using the colour code defined in (d). The arrow in (a), (b) and (c) shows two grains that were identified as one that is a result of a missing phase boundary (see discussion).

for the EBSD grain maps (about 42% smaller compared to the SEM micrographs value). This is a consequence of the identification of α-Zr grain boundaries that are not seen in the SEM micrographs because the preparation technique reveals only the β′-Zr phase. In the radial direction, the minor axis length was found to be about 20% smaller for the EBSD grain maps compared to the SEM micrographs. This can be explained by the over-estimation of the β′-Zr phase in the extrapolation procedure due to the non-indexing of the α-Zr phase on the phase boundaries. However, it confirms that both techniques are able to correctly identify phase boundaries. Table 2 also shows that the aspect ratio is indicative of more circular α-Zr grains coming from the EBSD grain maps analysis.

3.5. Correlation between micro-texture and micro-structure using EBSD grain maps

Table 3 presents the proportion of grains obtained using EBSD grain maps which have their long axis in the radial and tangential direction. This measurement is compared to the orientation of the basal plane normal of the hcp crystal structure made on every point during EBSD measurements using the equation

$$F_d = \sum_{\theta} V(\theta)\cos^2\theta, \qquad (1)$$

where d is the direction (radial, tangential, axial) and $V(\theta)$ is the volume fraction of the material with its c-axis (basal plane normal) at an angle θ from the direction d.

Table 3 compares the alignment computed using grain size orientation and compares it to the crystal orientation measurement. First, the F_d's obtained from the orientation of individual grains by EBSD measurement are in very close agreement to the expected values reported by Holt [3] using XRD measurements from a series of standard Zr–2.5Nb pressure tubes (from offcuts). It is also very interesting to note the good correlation between the F_x (radial) computed using the direction of the basal plane (crystallographic data) and the grain long axis data obtained using the grain map as determined by EBSD and computed using the HKL Channel 5 ellipse fit. This proves that the basal normal direction follows the direction of the long axis of the grains. Hence, an estimate could be obtained of the amount of texture (micro-texture) of the pressure tube without any crystallographic measurements along the radial direction. This measurement could be more easily performed than using collimated XRD apparatus.

However, computing grain orientation using the phase maps does not compute for the F_z (axial) direction since measurements are only made on the radial–tangential plane. Nevertheless, the texture ratio, $Z = F_{\text{radial}}/F_{\text{tangential}}$, or texture difference, $F_{\text{tangential}} - F_{\text{radial}}$, could still be estimated, which is often used in the

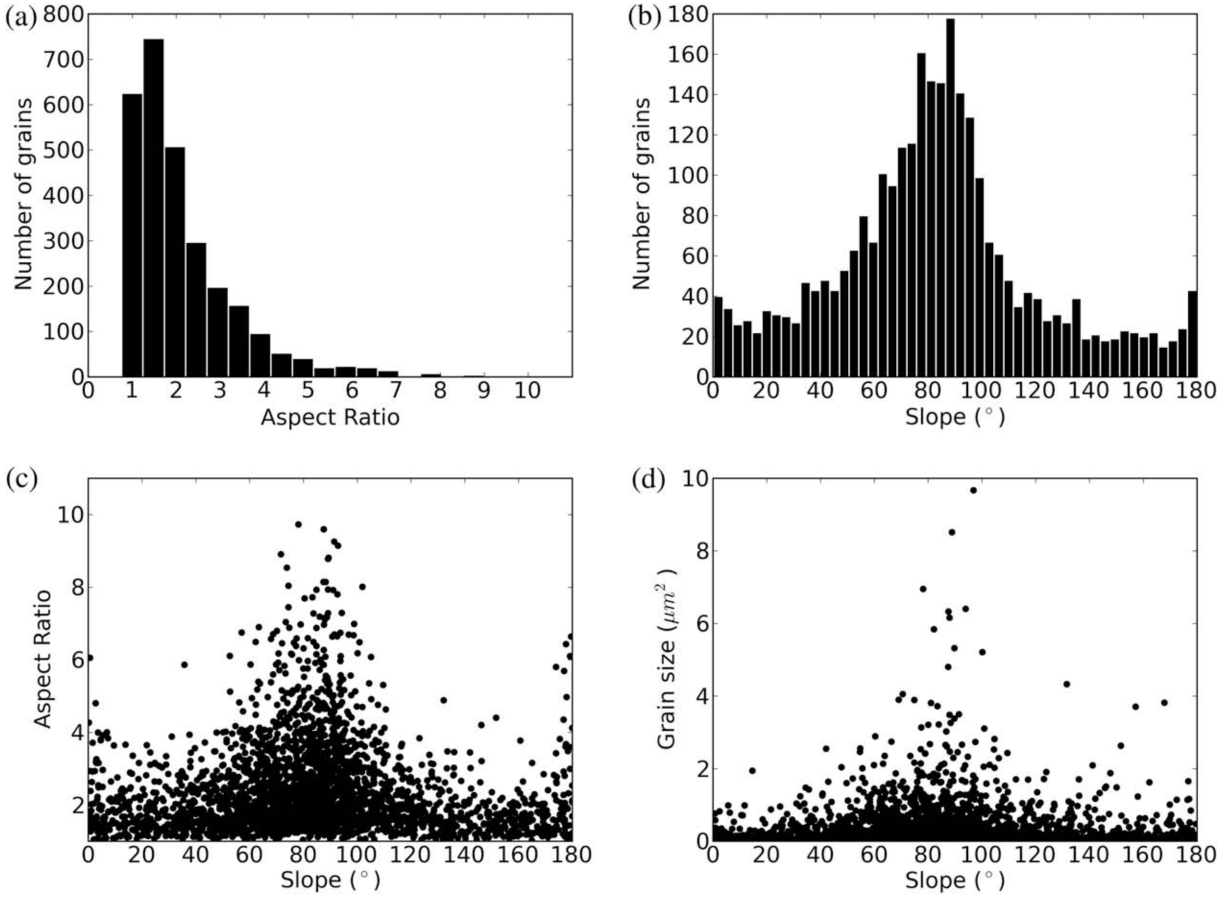

Fig. 9. Aspect ratio (a) and (b) long axis angle distribution vs the radial axis of the fitted α-Zr grains (all regions). The aspect ratio (c) and grain size (d) are also presented as a function of grain orientation.

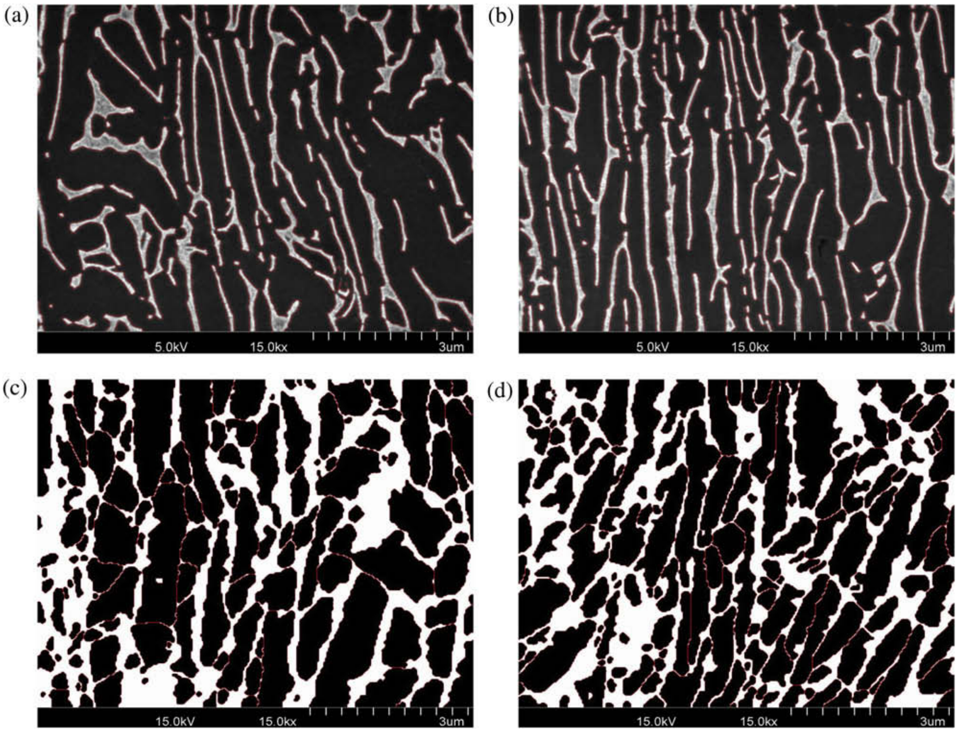

Fig. 10. Typical micrographs used for the intercept methods using electron micrographs at 5 kV ((a) and (b)) and binary image of the grain map as calculated based on EBSD measurements ((c) and (d)). Images were taken from the same sample in approximately the same area.

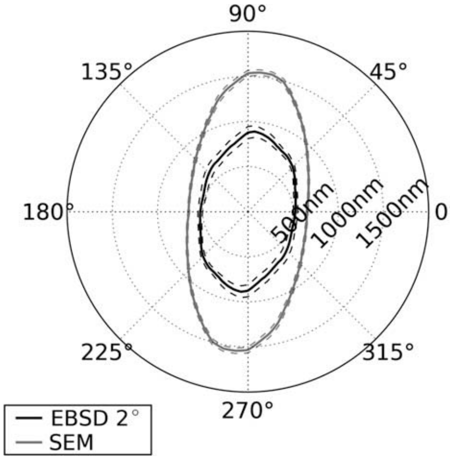

Fig. 11. Average intercept length as a function of direction (x = radial; y = tangential) calculated using image analysis and grain map of EBSD measurements using the same algorithm. The dashed lines show the 95% confidence interval on the average intercept. For more information, see Lagace et al. [7].

Table 2
Half minor and major axis length and aspect ratio of the average intercept length plotted in Fig. 11 using the EBSD grain map and SEM micrographs.

	EBSD grain maps	SEM micrographs
1/2 minor axis length (nm)	519	654
1/2 major axis length (nm)	890	1547
Aspect ratio	1.71	2.36

Table 3
F_d of the basal plane (0 0 0 1) measured by EBSD texture information compared to the one calculated using the direction of the long axis of the fitted ellipse and the reported value from Holt [3] (front offcut).

F_d direction	EBSD-texture, (c-axis direction, this work)	EBSD-grain direction, (grain long axis, this work)	XRD measurement [3] (front offcut)
F_x (radial)	0.298	0.3	0.298 ± 0.025
F_y (tangential)	0.646	0.7	0.642 ± 0.031
F_z (axial)	0.055	Not available	0.057 ± 0.017

correlation between in-service behavior and the texture of Zr–2.5Nb pressure tubes [3].

However, it was not possible for the SEM micrographs, using our actual image analysis algorithm, to determine values of F_d since no information on individual α-Zr grains is computed. We are trying to develop new algorithms in order to compute values for F_d. It will then be possible to determine the local variation of the 'texture' in the radial and tangential direction using a relatively fast technique.

In addition, using the raw EBSD results (un-extrapolated), the microstructure could be correlated with the expected texture of the Zr–2.5Nb [17]. Fig. 12 presents the phase colour according to the components of the three textures. Type I (red), which is the result of the deformation of the original (prior) α-Zr (<40% by volume), has a basal normal direction predominantly in the radial direction (maximum deviation set at 40° to the radial direction). Type II (green) is believed to be stress-induced β-Zr → α-Zr phase transformation (>60% by volume), with a basal normal direction predominantly in the transverse direction (maximum deviation set at 40° to the transverse direction). Finally, type III (blue) is the result of β-Zr → α-Zr phase transformations occurring after extrusion during cooldown and has a basal normal direction predominantly in the axial direction (maximum deviation fixed at 40° to the axial direction). Using this technique, we can clearly identify the α-Zr associated with each component and determine the difference in grain morphology for each type. Type I is more equiaxed. Type II is more elongated towards the transverse direction. Type III, which corresponds α-Zr phase transformed after extrusion during the cooldown, is formed of smaller grains, as expected. Using the complete map (18 regions), we calculated that type II constitutes the major component (65%), followed by type I (24%) and type III (3%). Those values are in close agreement with Griffiths et al. [17]. Only 8% of all the α-Zr grains have an orientation outside these three limits (>40° deviation). The most important deviation is coming from type I-radial (24% vs. 29.8% computed using the direction of the c-axis and type III-axial (3% vs. 5.5% (Table 3).

It is also possible to independently compute the grain size distribution for the three grain textures. Fig. 13 shows the distribution of grain size (in μm^2) for the type I, II and III grains. The type I and type II grain size distributions are shown to be different after 0.4 μm^2, after which the type II grains show a lower decrease than their type I counterparts. This suggests the use of two different log-normal functions for modeling grain size distribution rather than one. Fig. 13 also shows that type III grains have a much smaller grain size.

4. Discussion

4.1. Maximal indexation

The Zr–2.5Nb pressure tube has a relatively fine microstructure. Hence, the indexation rate of EBSD patterns, because of overlapped or diffuse patterns, will be lower than usually expected when performing grain mapping with EBSD (>85% indexation rate for less than 10% error in grain size [13]). Hence, it is important to assess EBSD indexation limits based on phase content and resolution limits.

The average indexation percentage of the α-Zr phase obtained from the 'as acquired' EBSD maps is about 70%. The remaining 30% includes the β-Zr phase (∼1%), but mainly non-indexed patterns around the α-Zr phase. As mentioned previously, we were not able to identify the β′-Zr phase in our EBSD measurement.

To evaluate the surface fraction of the β′-Zr phase, secondary electron images of the sample prepared for image analysis were used. Because of the sharp contrast between the α-Zr and β′-Zr phases, we can more easily resolve the boundaries between the two phases as well as their surface fraction. Images were taken at high magnification (50 kX). A pixel dimension of about 2 by 2 nm was obtained, which is much smaller than the 30 by 30 nm pixels from the EBSD maps. The average β′-Zr surface fraction over 250 images is 15.4%. The identified boundaries between the two phases are shown by a red line in Fig. 14. Since the secondary electron images and EBSD maps were taken from approximately the same region on the same sample, it can be assumed that 15.4 of the 30% of non-indexed pixels is due to the β′-Zr phase. Hence, we found that the indexation rate experimentally obtained for the α-Zr is ∼83% (70/84.6).

4.2. EBSD effective spatial resolution

Another factor influencing the indexation is the effective resolution of the EBSD measurement. Because of the asymmetric electron interaction volume due to the high tilt angle of the surface, the resolution in the parallel direction to the tilt axis is about three times better than the one in the perpendicular direction [3,18]. To minimize the effect of the asymmetric resolution, the sample was

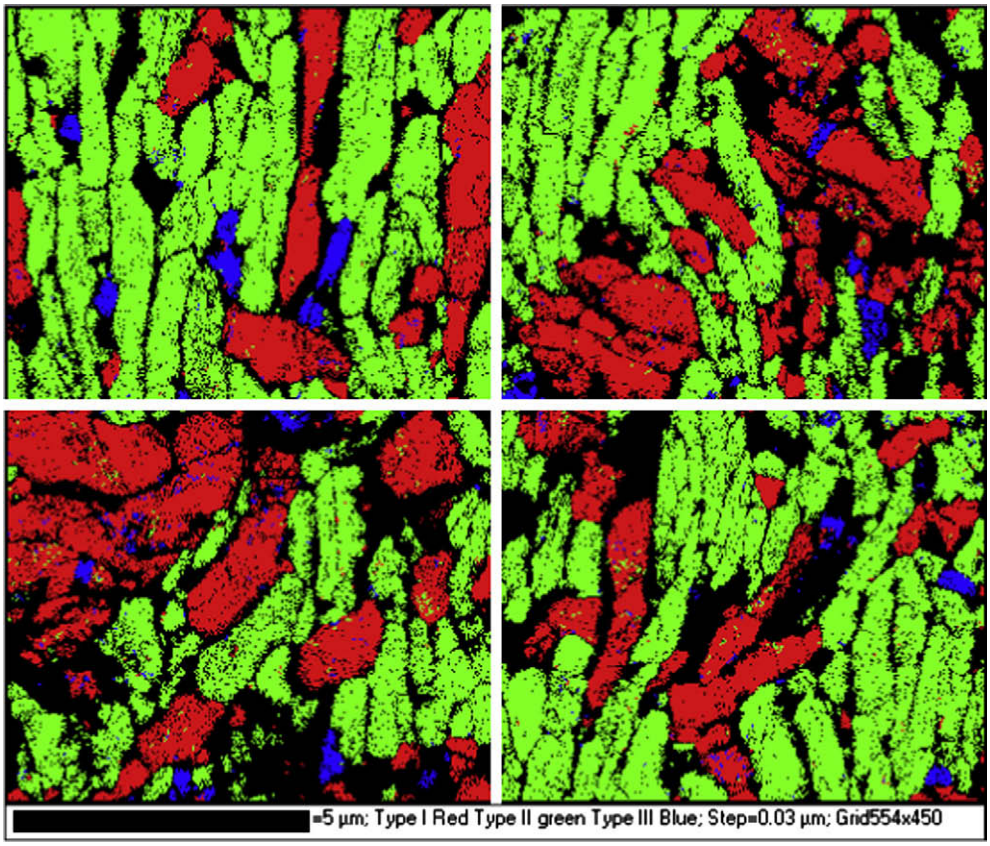

Fig. 12. Colour map showing the three α-Zr components. Type I (Red, grains with the (0 0 0 1) plan normal less than 40° of the radial direction), type II (green, grains with the (0 0 0 1) plan normal less than 40° of the transverse direction) and type III (blue, grains with the (0 0 0 1) plan normal less than 40° of the axial direction).

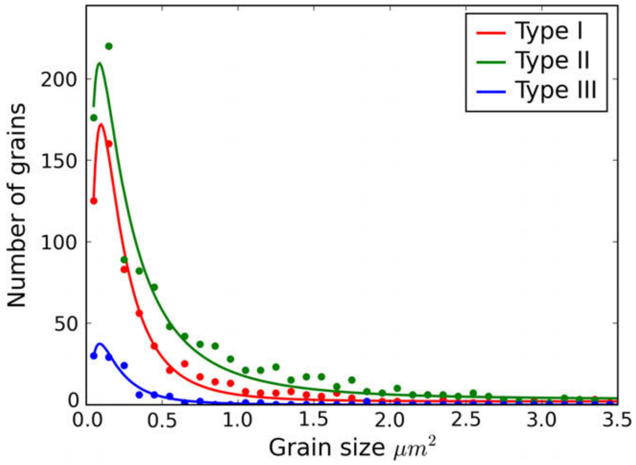

Fig. 13. Grain size distribution of type I (deformed original (prior) α-Zr), type II (stress-induced β-Zr → α-Zr phase transformation) and type III (β-Zr → α-Zr phase transformations occurring after extrusion during cool down) α-Zr grains. We present also a logarithm fit of the type I, II and total distribution function.

aligned so that the elongated Zr–2.5Nb grains are perpendicular to the tilt axis for all EBSD maps. This corresponds to a tilt axis parallel to the radial direction of the tube. Using this surface orientation, most phase boundaries are better resolved.

To assess the resolution effect on the indexation percentage, the β′-Zr phase was enlarged using an anisotropic dilation (height-wise expansion is three times greater than width-wise expansion along the image). A typically reported effective resolution value in the parallel direction to the tilt axis for a cold field emission gun is 10 nm (pure iron) [13]. Applied on the β′-Zr phase, this resolution is equivalent to an increase of 3.5% of this phase (yellow line in Fig. 14(a)). Therefore, it can be expected that 18.9% (15.4 + 3.5%) of the pixels on the EBSD maps may not be indexed because of added effect of resolution limit. However, only the resolution effect on phase boundaries was considered in this calculation since grain boundaries within the α-Zr phase are not visible in the secondary electron images. The presence of grain boundaries will certainly increase the number of non-indexed pixels due to the resolution limits. However, we were not able to quantify it using SEM micrographs.

By combining the surface fraction of the β′-Zr phase (15.4%) and the 10 nm resolution (3.5%), we found that at least 18.9% of EBSD patterns will not be indexed. This is significantly lower than the 30% of non-indexed pixels found experimentally. By uniformly increasing the β′-Zr phase in the secondary images to reach 30%, this was equivalent to having a 36 nm gap around the phase boundaries (green line in Fig. 14(a)). In the EBSD maps, this corresponds to having α-Zr grains with approximately one non-indexed pixel around their perimeter since a step size of 30 nm was used. On the other hand, as reported by Rolland et al. [19], higher strain concentrations around grain boundaries can diminish the detection limits. For a second method, we used an anisotropic dilation that is performed directly on the β′-Zr phase until it occupies 30% of the surface, with the β′-Zr phase being increased by 42 nm radially and 126 nm tangentially (Fig. 14(b)). It is interesting to note that the two computed resolution values for the phase boundary (36 + 10 nm for isotropic and 42 nm for anisotropic) are in close agreement.

For elongated grains with their width approximately aligned in the direction of the tilt axis, the minimum detection limit would be

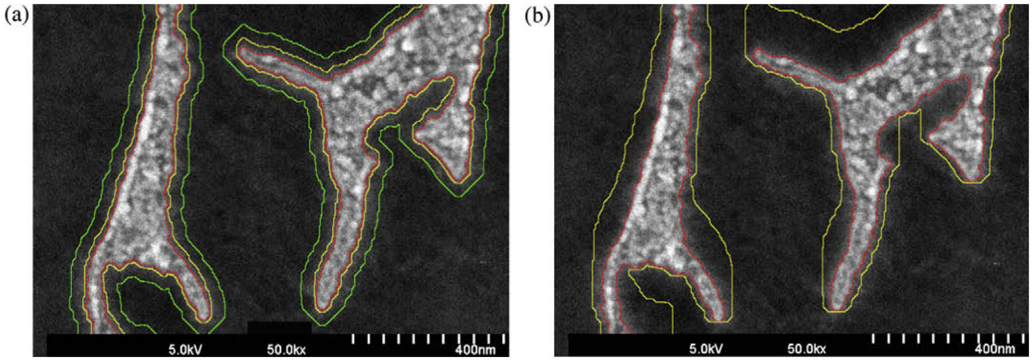

Fig. 14. SEM micrographs showing the β′-Zr phase in white and α-Zr phase in black. The red line corresponds to the phase boundary between the α-Zr and β′-Zr phases. (a) The yellow line is the phase boundary corrected for an anisotropic effective resolution of 10 nm by 30 nm and the green line indicates the equivalent area for 30% of non-indexed pixels in the EBSD maps. (b) The yellow line is the phase boundary corrected for an anisotropic effective resolution of 42 nm by 126 nm.

approximately 83 nm (10 + 2 × 36 nm or 2 × 42 nm). Knowing that the tangential resolution is 1/3 of the lateral (radial) resolution, a minimum grain area of 0.02 μm^2 (83 × 249 nm) can be calculated. This limit depends on the experimental conditions used for the EBSD acquisitions. For instance, surface roughness at boundaries caused by the sample preparation could worsen the resolution and lead to a lower indexation rate. It is important to note that improvements in sample preparation would allow an increase in the quality of the diffraction patterns as well as a faster and more accurate indexation of every pattern. A smaller step size could possibly have led to a better definition of the phase and grain boundaries, but to the detriment of the acquisition time or the area covered by the maps. The step size, magnification, sample preparation method and other experimental conditions were carefully optimized to detect α-Zr grains with enough statistics to perform a grain analysis and prevent acquisition artifacts such as drift and contamination that could affect the results. Lastly, the effective resolution is dependent on the ability of the indexing algorithm to correctly identify overlapping patterns, and since the unwrap pattern is being used, this could worsen the indexing rate of the HKL software.

4.3. Extrapolation algorithm

The main challenge in the microstructural analysis of Zr–2.5Nb pressure tubes using EBSD arises from the fact that it is difficult to find a specimen preparation technique that gives good EBSD patterns of both the main phase (α-Zr) and the secondary phases (constituents of β′-Zr). In addition, because those secondary phases are intertwined, can contain a high density of dislocations and are very small, it is possible that the indexation of such phases can never be achieved with the SEM. The TEM could be used but the area covered for the analysis would be very small and could be less representative considering the level of anisotropy of this particular microstructure. It would also be possible to grow and stabilize the non-α-Zr regions with a heat treatment. However, this procedure will affect the overall microstructure and perhaps even the micro-texture.

On the other hand, in the SEM micrographs used for image analysis, the phase boundaries between the α-Zr and β′-Zr phases are more clearly seen but fail to reveal any α-Zr grain boundaries. Hence, a combination of both techniques is a step toward a more complete microstructural analysis of Zr–2.5Nb pressure tubes.

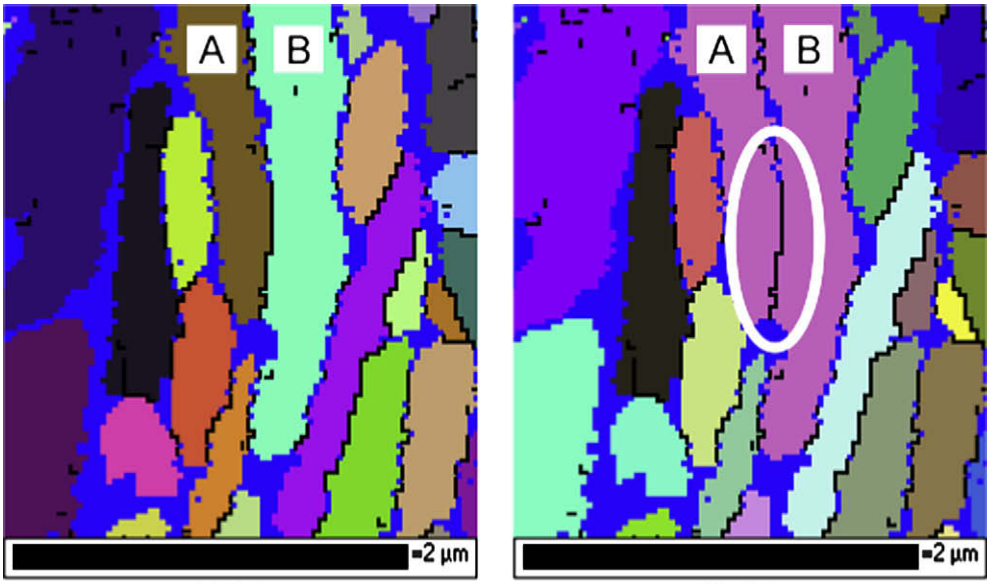

(a) 2 deg (b) 5 deg

Fig. 15. Random colour grain map using a criterion of (a) 2° and (b) 5° to differentiate between two grains. The β′-Zr phase is coloured blue. In (b), we can clearly see that two grains separated by the β′-Zr phase are joined together because the β′-Zr was not identified completely and the two adjacent grains share approximately the same orientation.

Extrapolation of non-indexed EBSD patterns could create some bias and one must proceed cautiously. In this work, it was assumed that a secondary phase must separate two distinct α-Zr grains. In other words, there is no β′-Zr phase within a single α-Zr grain. Therefore, a group of pixels with a similar orientation separated by a region of β′-Zr corresponds to two individual grains. Those two grains can have very similar orientations (less than 5°) since extruding creates a lot of grains with similar orientations. The boundary between them is caused by the presence of a second phase. The inability to properly resolve small β′-Zr grains between the α-Zr grains leads to the blending of grains that are in fact distinct according to our definition. The latter definition seems to give an equivalent grain representation to TEM thin foil [5]. Nevertheless, to obtain a more realistic grain structure representation, a complete 3D representation of the microstructure must be done. Work is now underway using Z-slices in dual-beam microscopes (focused ion beam and electron beam) to more completely reveal the microstructure and the interconnectedness of α-Zr and β′-Zr.

A random colour grain map using a criterion of (a) 2° and (b) 5° of mis-orientation to differentiate between grain A and B is seen in Fig. 15(a). The β′-Zr phase is shown in blue. In (b) we can see that two grains separated by some β′-Zr phase are joined together because this β′-Zr phase was not properly identified and the two adjacent grains share approximately the same orientation. Hence, in order to distinguish grains with almost the same orientation but separated by a phase boundary, very low mis-orientation criteria are used for grain definition (2°). Usually a 2° mis-orientation to define a grain boundary is classified as low angle boundaries and used for sub-grain structure [13]. This definition provides good results for distinguishing α-Zr separated by a phase boundary (mainly in the short or radial direction). This can be seen by the fact that the difference between the average intercept lengths of SEM micrographs and the EBSD phase map intercept length is smaller in the short axis dimension (radial direction) (Table 2) than along the long axis direction (tangential direction). This is a consequence of the EBSD grain maps being able to reveal α-Zr grain boundaries which cannot be seen in the SEM micrographs since our specimen preparation only etched the β′-Zr phase. Elongated regions (long intercept length on average) observed in the SEM micrographs appear truncated in the EBSD grain maps because they contain more than one grain.

It is important to note that there could be some oversegmentation in the tangential direction since a small mis-orientation grain boundary criterion is being used (<2°). Fig. 16(a) shows a BC map of a selected area and a corresponding phase map with grain boundaries at 2° and less, between 2° and 5° and higher than 10° of mis-orientation. The BC maps reveal a sub-structure inside the α-Zr grain that does not appear with the SEM micrographs. It is clear that EBSD grain maps reveal much more detail in the α-Zr phase than the SEM micrographs. We can also see that several α-Zr grains can contain grain boundaries at relatively high mis-orientation angles (>10°).

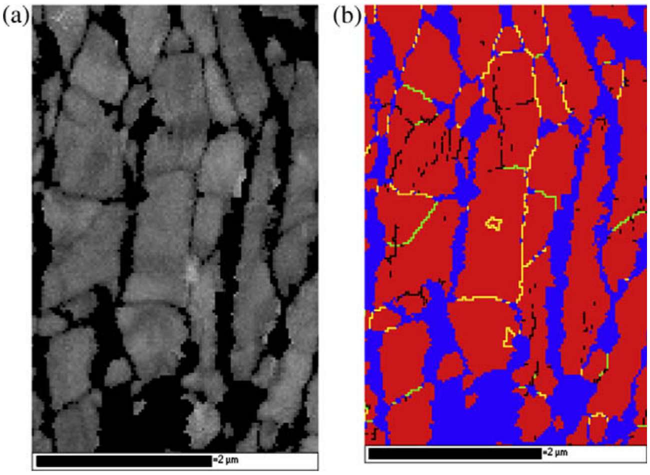

Fig. 16. (a) BC maps of a selected area. In (b) we present a phase map (blue = β′-Zr; red = α-Zr) that also shows grain boundaries with a difference of less than 2° (black), between 2° and 5° (green) and higher than 10° (yellow) between adjacent regions.

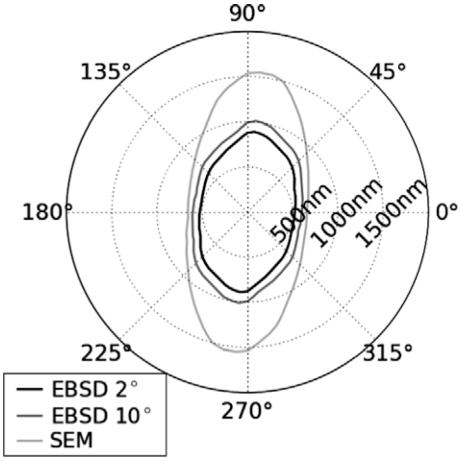

Fig. 17. Average intercept length as a function of direction (x = radial; y = tangential) calculated using image analysis and a grain map of EBSD with a mis-orientation grain boundary criterion of 2° and 10°.

This argument is further reinforced by looking at the average intercept length ellipse performed on the same EBSD grain maps but with a mis-orientation grain boundary criterion of 10° (Fig. 17). Both the minor and major axis lengths are increased. The former is due to the fact that, as shown in Fig. 15, with a high mis-orientation grain boundary criterion, some α-Zr grains become merged. The average intercept length along the radial direction is therefore increased. More interestingly, the major axis of the 10° ellipse is still significantly shorter (35%) than the one from the SEM micrographs. The presence of grains in α-Zr regions is not an artefact of the grain boundary definition, but the illustration of the true microstructure.

5. Conclusions

Microstructural characterization is an important facet for understanding the creep behavior of in-service pressure tubes aimed at achieving better end-of-life prediction and for increasing predictability and better profitability of CANDU reactors. SEM micrographs and EBSD grain maps provide complementary results on the microstructure of Zr–2.5Nb pressure tubes.

It was shown that EBSD can be used to characterize the grain shape and orientation of α-Zr grains. Due to the limitations of detecting the β-Zr, ω-Zr and other small phases, an extrapolation technique based on the band contrast and a low mis-orientation angle criterion were successfully used to fill out the non-indexed regions and detect α-Zr grains. It was shown that a high angle boundary (>10°) is present inside α-Zr lamellae. Grain size analysis based on EBSD grain maps indicate that the actual α-Zr size are smaller and have a more rounded shape than what is normally obtained using image analysis combined with an intercept method of SEM micrographs. It was also shown that types I and II grains exhibit a different grain size distribution and that two different log-normal equations should be fitted to the total grain size distribution.

The orientation and distribution of the α-Zr lamellae are more easily obtained using the SEM micrographs because this technique is capable of detecting the β′-Zr phase. The acquisition of the micrographs is faster, requires less labour-intensive sample preparation and covers a much wider area than EBSD measurements. More than 100 images can be taken in the same amount of time as one EBSD map. However, EBSD grain maps provide detailed information about the internal structure of the α-Zr lamellae (grains, grain boundary, local misorientation, etc.) as well as the possibility of correlating the microstructure to the micro-texture.

Acknowledgements

We would like to thank Jennifer Cocle for her useful comments on the proofreading of this paper and with some of the aspects of specimen preparation. The technical support and scientific discussion by George Vander Voort have been invaluable for our work. His knowledge and expertise combined with his enthusiasm make any scientific collaboration with him a unique experience.

References

[1] C.E. Coleman, in: G.D. Moan, P. Rudling (Eds.), Zirconium in the Nuclear Industry: Thirteenth International Symposium, ASTM STP 1423, ASTM International, West Conshohocken, PA, 2002, p. 3.
[2] D.G. Hurst et al., Canada Enters the Nuclear Age: A Technical History of Atomic Energy of Canada Limited as Seen from Its Research Laboratories, McGill-Queen, 1997.
[3] R.A. Holt, J. Nucl. Mater. 372 (2008) 182.
[4] R. McCabe, E.K. Cerreta, A. Misra, G.C.N. Tome, Philos. Mag. 86 (2006) 3395.
[5] M. Griffiths, W.G. Davies, A.R. Causey, G.D. Moan, R.A. Holt, S.A. Aldridge, in: G.D. Moan, P. Rudling (Eds.), Zirconium in the Nuclear Industry: 13th International Symposium, ASTM STP 1423, ASTM International, West Conshohocken, PA, 2002, p. 796.
[6] M. Griffiths, J.E. Winegear, Atomic Energy of Canada Ltd., Report AECL-10835, 1994.
[7] M. Lagace, L. Rodrigue, P. Hovington, M.L. Trudeau, J. Met. (JOM) 60 (4) (2008) 17.
[8] R.A. Holt, P. Zhao, J. Nucl. Mater. 335 (2004) 520.
[9] Automatic Sample Preparation (ASaP) is a trade mark of EA Fischione Instrument (www.fischione.com).
[10] G.F. Vander Voort, W. Van Geertruyden, Buehler Ltd., 2006.
[11] G.J.C. Carpenter, J.A. Jackman, J.P. McCaffrey, R. Alani, J. Microsc. Soc. Am. 1 (4) (1995) 175.
[12] R.J. McCabe, G. Proust, E.K. Cerreta, A. Mistra, Int. J. Plasticity, in press. doi:10.1016/j.jiplas2008.03.010.
[13] F.J. Humphreys, J. Mater. Sci. 36 (2001) 3833.
[14] G.F. Vander Voort, Buehler Ltd., Lake Bluff, personal communication.
[15] Lispix, version lx92p (<www.nist.gov/lispix/doc/contents.htm>). D.S. Bright, K. G. Milans+, Surface and Microanalysis Science Div., Nat'l Inst. of Stds. and Technology, Gaithersburg, MD. 20899-8371, Undergraduate Dept. of Computer Science, Carnegie Mellon University, Pittsburgh, PA.
[16] Images Analysis Software (RML-Image) is freely available on the web (www.rml-image.com).
[17] M. Griffiths, R.A. Holt, J. Li, S. Salmoto, Microstruct. Sci. V26 (1998) 293.
[18] T.C. Isabell, V.P. Dravid, Ultramicroscopy 67 (1997) 59.
[19] P. Rolland, K.G. Dicks, C.T. Chou, Mater. Sci. Forum 408–412 (2002) 535.